NeuroImage 43 (2008) 69–80

Contents lists available at ScienceDirect

NeuroImage

journal homepage: www.elsevier.com/locate/ynimg

On the construction of an inter-subject diffusion tensor magnetic resonance atlas of the healthy human brain

Wim Van Hecke [a,b,*], Jan Sijbers [a], Emiliano D'Agostino [c], Frederik Maes [c], Steve De Backer [a], Evert Vandervliet [b], Paul M. Parizel [b], Alexander Leemans [d]

[a] Visionlab (Department of Physics), University of Antwerp, Antwerp, Belgium
[b] Antwerp University Hospital (Department of Radiology), University of Antwerp, Antwerp, Belgium
[c] Medical Image Computing (Department of Electrical Engineering (ESAT)), K.U. Leuven, Leuven, Belgium
[d] CUBRIC (School of Psychology), Cardiff University, Cardiff, UK

ARTICLE INFO

Article history:
Received 24 January 2008
Revised 6 June 2008
Accepted 2 July 2008
Available online 18 July 2008

Keywords:
Diffusion tensor imaging
Non-rigid coregistration
Inter-subject group atlas
Diffusion tensor tractography

ABSTRACT

Voxel based morphometry (VBM) has been increasingly applied to detect diffusion tensor (DT) image abnormalities in patients for different pathologies. An important requisite for a robust VBM analysis is the availability of a high-dimensional non-rigid coregistration technique that is able to align both the spatial and the orientational DT information. Consequently, there is a need for an inter-subject DTI atlas as a group specific reference frame that also contains this orientational DT information. In this work, a population based DTI atlas has been developed that incorporates such orientational DT information with high accuracy and precision. The proposed methodology for constructing such an atlas is compared with a subject based DTI atlas, in which a single subject is selected as the reference image. Our results demonstrate that the population based atlas framework is more accurate with respect to the underlying diffusion information.

Introduction

Diffusion tensor magnetic resonance imaging (DT-MRI or DTI) is becoming increasingly important in neuroscience research since it can probe the structure and properties of the brain white matter (WM) tissue in vivo and non-invasively (Basser et al., 1994). The potential of DTI to expose WM pathways, consisting of axon bundles, is based on the fact that water molecules have a larger probability to diffuse along the axonal structures than perpendicular to them (Beaulieu, 2002). The virtual reconstruction method of WM pathways, also referred to as diffusion tensor tractography, is becoming a valuable diagnostic tool for a large number of neuropathological diseases (Bammer et al., 2003; Toosy et al., 2003; Abe et al., 2004; Pagani et al., 2005). In addition, quantitative diffusion properties have shown to be sensitive markers for studying a wide range of WM altering pathologies (Rovaris and Filippi, 2007; Fellgiebel et al., 2007). In this context, the fractional anisotropy (FA), which is a normalized measure of the degree of anisotropy, and the mean diffusivity (MD), i.e. the averaged amount of diffusion, are generally examined.

Diffusion parameter alterations are commonly detected by a user-defined region of interest (ROI) analysis, requiring a manual or semi-automatic segmentation of the structures of interest (Snook et al., 2005). Such ROI measurements can be quite laborious and can be confounded by a lack of reproducibility due to an inter- or intra-operator variability in the delineation of the ROIs. Furthermore, a ROI analysis can only detect diffusion parameter differences in regions that were a priori hypothesized to be associated with the studied WM disorder. Also, the spatial location and the extent of diffusion tensor parameter differences are generally not known in advance. Therefore, an increasing number of studies incorporate voxel-based morphometry (VBM) strategies evaluate changes in diffusion of WM altering pathologies (Ashburner and Friston, 2000). In a VBM analysis, statistical tests are performed for each voxel separately. Hence, the whole brain is checked for patient–control differences, without any a priori hypothesis being made about the spatial location and extent of the parameter alterations.

An important requisite for a reliable statistical analysis in a VBM study is that, after the DT image alignment to a common atlas space, spatially overlapping voxels of different subjects correspond to the same anatomical structure. It is generally assumed that affine transformations, which consist only of global translations, rotations, shearing, and scaling factors, cannot deal with the local morphological discrepancies between different subjects (Bürgel et al., 2006). In order to minimize local differences in brain shape across subjects non-rigid coregistration algorithms are required. However, since the local variability of the human brain across subjects can be very large,

* Corresponding author. Visionlab Department of Physics, University of Antwerp, Universiteitsplein 1, N 1.18, B-2610 Antwerp, Belgium. Fax: +32 3 820 22 45.
E-mail address: Wim.Vanhecke@ua.ac.be (W. Van Hecke).

1053-8119/$ – see front matter © 2008 Elsevier Inc. All rights reserved.
doi:10.1016/j.neuroimage.2008.07.006

image alignment inaccuracies may be present after the non-linear warping of the images to atlas space, potentially affecting the VBM statistics (Bookstein, 2001; Jones et al., 2007). In addition, the coregistration of DT images is particularly challenging compared to aligning scalar images, since in DT images each voxel is represented by a symmetric second rank tensor, i.e. the six components describing the three-dimensional diffusion process (Basser and Pierpaoli, 1996).

It has been reported that small spatial alignment inaccuracies, which may be present after the non-rigid coregistration, can introduce substantial tensor reorientation errors. However, several studies have shown that incorporating all DT information during coregistration and applying an appropriate tensor reorientation strategy can improve both the spatial and orientational DT image alignment (Park et al., 2003; Van Hecke et al., 2007; Alexander et al., 2001). Consequently, a single subject or an atlas that is going to be used in a DTI VBM analysis as a reference image for coregistration should also contain this multi-component DT information.

Most VBM studies utilize a standard reference image, such as the Montreal Neurological Institute (MNI) atlas, which was constructed from the affine transformation of 305 MR images of normal subjects to the stereotactic space defined by Talairach and Tournoux (1988). The advantage of a standard template such as the MNI atlas is that it contains coordinate, anatomic, and cytoarchitectonic labels and that the VBM results can be compared in a standard way across many studies that employed the this atlas. However, since this atlas is not study-specific, it might fail to provide a good representation of the given population, thereby potentially resulting in alignment errors after coregistration of the study group images to this reference space. Furthermore, since the MNI atlas is an MR atlas, many DTI based VBM studies utilize only the T_2 weighted image information of different subjects to drive the coregistration to the MNI space. This introduces WM alignment errors, because no DT information is considered during the warping procedure (Park et al., 2003). In some studies, the deformation field which was acquired by the coregistration of anatomical MR images is subsequently applied to the FA maps to create an FA template, whereto all data sets are warped (Kyriakopoulos et al., 2007).

In other VBM studies, a single subject data set of the image group is selected as the reference or template image (Jones et al., 2002; Smith et al., 2006; Douaud et al., 2007). Although such an atlas is study-specific, it might fail to be a good representative of the whole subject group. Furthermore, the unique brain topology of this single subject can differ significantly from the brain topology of the other subjects in the image group, especially when patients with certain WM disorders are included in the analysis. Guimond et al. (2000) introduced an atlas construction methodology based on the coregistration of all subjects to a single subject data set which is selected as the initial reference image, followed by the averaging of all these coregistered images in the space of this initial reference image. Finally, the resulting atlas is transformed with a deformation field that is equal to the average deformation of the initial reference image to all other images of the subject group. A previously reported disadvantage of this atlas construction method is that the resulting atlas can inherently contain unique features of the selected initial reference image, which results in a local topological bias (Wang et al., 2005).

During DTI atlas construction, Jones et al. (2002) incorporated FA maps for the affine coregistration of 10 subjects to a single subject image, which was previously transformed to the SPM T_2-weighted template. Wakana et al. (2004) created a WM and tractography atlas based on a high-spatial-resolution DTI data set. Dougherty et al. (2005) and Müller et al. (2007) used T_2-weighted and non-diffusion weighted images, respectively, for the image alignment during the atlas construction. Goodlett et al. (2006) applied the methodology of Joshi et al. (2004) to construct an atlas which was based on the alignment of scalar DT images. In their atlas method, the most representative template image is calculated as the data set that requires the minimum amount of transformation to each of the anatomical images. At each iteration, the updated template estimate is computed by the voxel-wise averaging of the deformed images. Ardekani and Sinha (2006) extended the atlas methodology that was developed by Guimond et al. (2000) to DT images, thereby using FA and MD images as information during the image alignment. Park et al. (2003) incorporated all DT information in their coregistration technique for the atlas construction, which was based on the methodology of Guimond et al. (2000). Other coregistration methods incorporate tensor reorientation as part of the image alignment optimization (Cao et al., 2005, 2006; Zhang et al., 2006). Zhang et al. (2007) incorporated tensor information during the image alignment to construct an atlas based on the method of Joshi et al. (2004).

In this work, a study-specific DT atlas is constructed whereby the magnitudes of the deformation fields that are needed to warp the different images to the atlas are minimized. This atlas is unbiased towards a single subject topology, since no single subject is selected as the initial reference data set. In addition, the directional diffusion information is reliably present in the DTI atlas model. Since it is very hard to objectively evaluate an atlas of a certain image group, a ground truth methodology is introduced to evaluate both the accuracy and precision of the spatial and orientational information in the atlas. In addition, inter-subject atlases are constructed based on the data sets of 20 healthy subjects to evaluate the different atlas frameworks in a realistic situation. Our results indicate that the atlas construction method affects the accuracy and the precision of the diffusion information in the final atlas.

Methods

Data acquisition

Diffusion tensor images of the brain were acquired with an 1.5 T MR scanner (Siemens, Erlangen, Germany) from 20 healthy subjects (8 males and 12 females), with a mean age of 25±3 years (19–30 years). An informed consent was signed by all participants.

Axial diffusion tensor images were obtained using an SE-EPI sequence with the following acquisition parameters: TR: 10.4 s; TE: 100 ms; diffusion gradient: 40 mT m^{-1}; FOV=256×256 mm^2; number of slices=60; voxel size=2×2×2 mm^3; b=700 s mm^{-2}; acquisition time: 12 min 18 s. Diffusion measurements were performed along 60 directions with 10 b_0-images for a robust estimation of FA, tensor orientation, and MD (Jones, 2004). DTI post processing, tractography, and visualization were performed with the diffusion toolbox 'ExploreDTI' (Leemans et al., 2005a). In this toolbox, the deterministic streamline fiber tracking approach is used for our purposes (Basser et al., 2000).

DTI coregistration

Global (affine) coregistration

In order to correct for global morphological differences, the DTI data sets were aligned to MNI space using an affine coregistration methodology. In this method, the FA images were used to estimate the affine transformation parameters, based on the maximization of mutual information (Maes et al., 1997).

For the remainder of the article, all images are considered to be aligned with an affine transformation to the MNI space, including a preservation of the principle direction (PPD) based tensor reorientation to realign the tensors with the underlying microstructure (Alexander et al., 2001).

Local (non-rigid) coregistration

After affine coregistration, the different images of the subject group were aligned using a recently developed non-rigid DTI coregistration technique (Van Hecke et al., 2007). In this coregistration approach, the images are modeled as a viscous fluid, which imposes constraints on the local deformation field during normalization

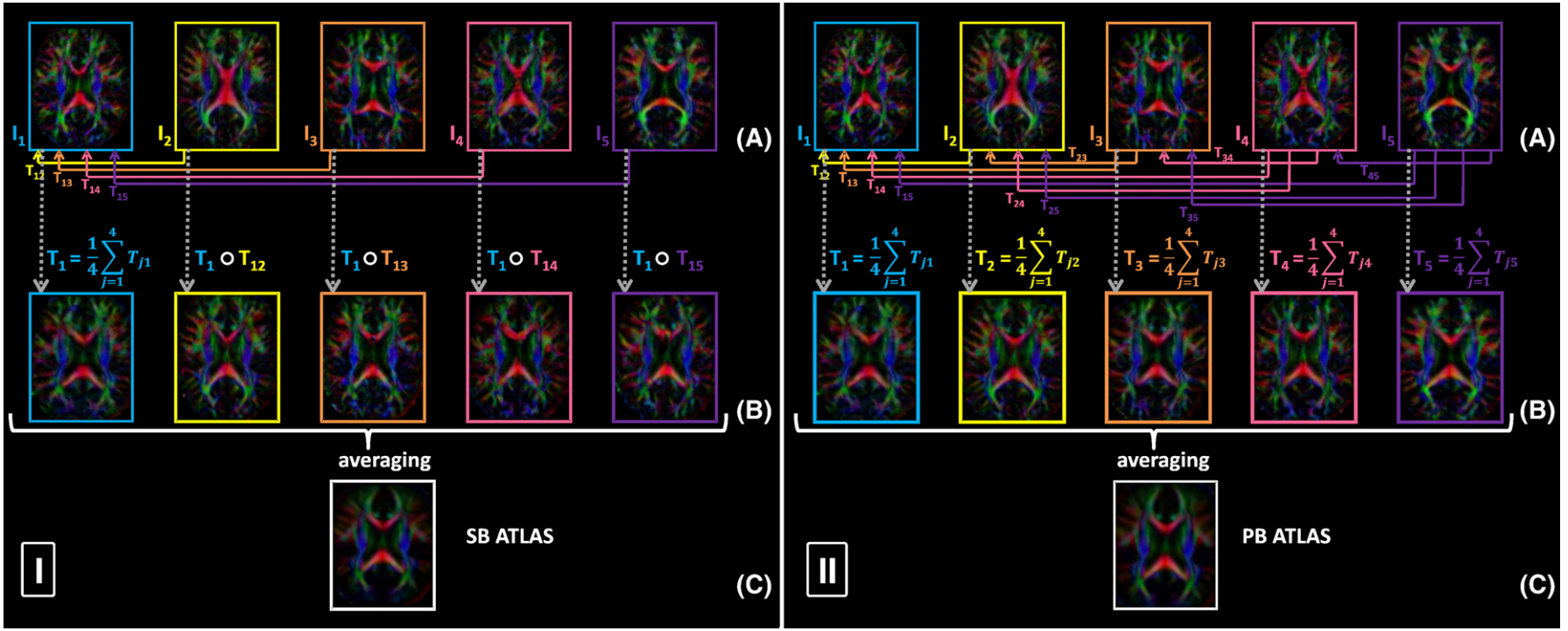

Fig. 1. A schematic overview of the subject and the population based atlas methodology is depicted for 5 DT images in I and II, respectively. In I(A) and II(A), the FA maps, color-encoded for the main diffusion direction, are shown after the affine deformation to the MNI space. In the subject based atlas framework, a single subject image is selected as the initial reference image (i.e., I_1 in this Figure). The deformation fields of all data sets to this reference image are calculated and denoted as T_{1j}, with $j=2, \ldots, 5$. In addition, the mean inverse deformation field$T_1 = \frac{1}{4}\sum_{j\neq 1} T_{j1}$ of the reference image to all other images is computed, with NS the number of subjects. Subsequently, as shown in (B), all images I_j are warped to the SB atlas space with a combined deformation field — containing the deformation field to the reference image, T_{1j}, and the mean deformation field of the reference image to the final atlas space, T_1. Finally the data sets in the SB atlas space are averaged to construct the SB atlas, as displayed in (C). In the population based atlas, non-rigid deformation fields are calculated between all images. Subsequently, for every image I_i, the mean deformation field T_i is calculated as the average transformation to all other images. This mean deformation field is applied to the corresponding data sets, including a tensor reorientation, resulting in the DT images of (B). The DW images of these data sets are averaged, resulting in the population based atlas, as represented in (C).

(D'Agostino et al., 2003). At each iteration, the determinant of the Jacobian is constrained to reduce the chance of forcing the underlying anatomical microstructure in an anatomically non-physical way. This viscous fluid model was optimized for the coregistration of multiple DTI information components (Van Hecke et al., 2007).

As mentioned by several investigators, tensor reorientation inaccuracies might be introduced after a non-rigid, high-dimensional transformation (Alexander et al., 2001; Van Hecke et al., 2007). These orientational alignment inaccuracies are caused by local coregistration errors that hardly affect the spatial alignment result, but on the other hand can have a severe impact on the accuracy of the subsequent tensor reorientation. In this context, it is important that the atlas construction framework minimizes this effect of the orientational alignment inaccuracies on the final atlas result.

DTI atlas construction

In the following sections, the multi-component DT images of the different subjects are denoted as I_i (with $i=1, \ldots, N_S$, and N_S the number of subjects). The deformation field that warps image I_j to image I_i, is then defined as T_{ij}. The proposed atlas construction framework, referred to as the population based (PB) atlas method, will be compared to the atlas construction framework of Guimond et al. (2000) which is referred to as the subject based (SB) atlas method. The latter method was utilized in the work of Ardekani and Sinha (2006) and Park et al. (2003) to construct a DTI atlas.

Subject based atlas method

The SB atlas methodology is based on the calculation of the non-rigid transformations T_{ij} of all data sets I_j to a specific data set I_i of the subject group, which was selected as the initial reference image. Thereafter, the mean deformation field of the initial reference image I_i to all other data sets I_j of the group (with $j=1, \ldots, N_S$) is computed as:

$$T_i = \frac{1}{N_S - 1} \sum_j T_{ji}. \quad (1)$$

This is the transformation of the initial subject space to the average space of the population. Next, all images I_j of the subject group are transformed with one deformation field – constructed as the consecutive application of the deformation fields T_{ij} and T_i, noted as $T_i \circ T_{ij}$ – directly to the final atlas space. This concatenation of deformation fields includes an interpolation of the vector fields.

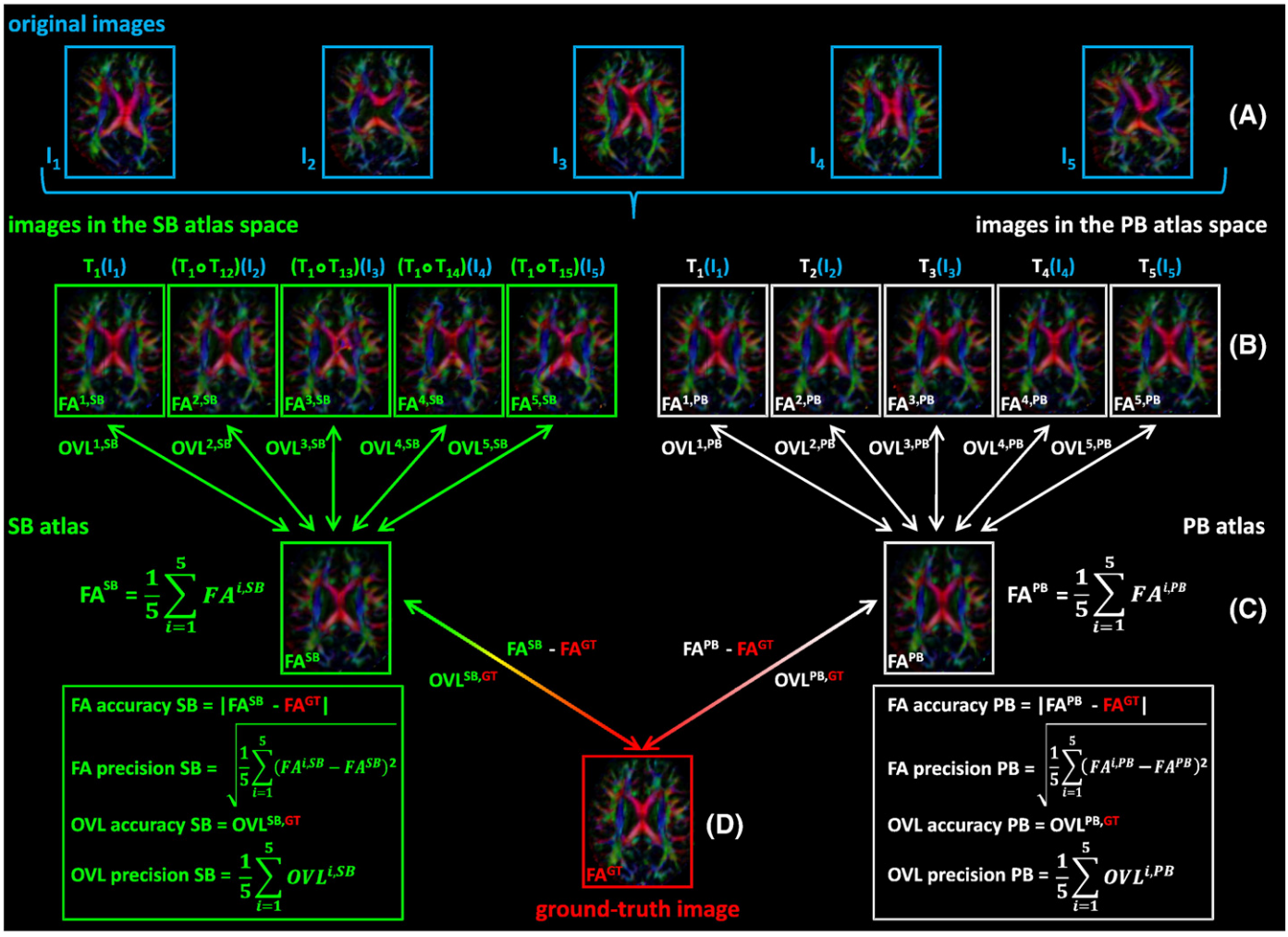

Fig. 2. In (A), the same axial slice of 5 different simulated data sets are displayed. These data sets are subsequently transformed to the SB and the PB atlas space with the appropriate deformation fields, as shown in (B), and averaged to construct the SB atlas and the PB atlas, as displayed in (C). The FA maps of the images in the SB and PB atlas space are denoted as $FA^{i,SB}$ and $FA^{i,PB}$, respectively ($i=1, \ldots, 5$), and the FA maps of the SB and the PB atlas are denoted as FA^{SB} and F A^{PB}, respectively. An axial slice of the golden standard data set is displayed in (D), and its FA map is denoted as FA^{GT}. The FA accuracy is calculated for each voxel as the absolute value of the FA difference between an atlas and the ground truth image. The OVL accuracy is computed as the OVL between an atlas and the ground truth image for each voxel, and denoted as $OVL^{SB,GT}$ and $OVL^{PB,GT}$ for the respective atlases. The FA precision of the SB and PB atlases is calculated as the standard deviation of the FA maps of the images in their respective atlas space. Finally, the OVL is computed between all images in a specific atlas space and its resulting atlas. This is denoted as $OVL^{i,SB}$ and $OVL^{i,PB}$ for the SB and the PB atlas, respectively ($i=1, \ldots, 5$). By averaging of $OVL^{i,SB}$ and $OVL^{i,PB}$ over the factor i, the OVL precision of the SB and the PB atlases is obtained.

Table 1
The median and interquartile range (IQR) of different quantitative evaluation measures for different atlases as evaluated with the ground truth methodology

	SB atlas		PB atlas	
	Median	IQR	Median	IQR
C	0.221	0.046	0.152	0.034
FA accuracy	0.094	0.089	0.067	0.061
FA precision	0.052	0.041	0.049	0.035
OVL accuracy	0.983	0.038	0.994	0.011
OVL precision	0.931	0.082	0.976	0.040

However, by combining the two non-rigid transformations, only one image interpolation and tensor reorientation step is now included to construct the final atlas.

$$\tilde{I}_j = \left(T_i \circ T_{ij}\right)\left(I_j\right) \quad (j = 1, \ldots, N_S). \tag{2}$$

After transformation of the DWIs to the atlas space, a PPD based tensor reorientation is performed to realign the tensors with the underlying microstructure (Alexander et al., 2001). Subsequently, the DWIs are recalculated from these reoriented diffusion tensors, in order to obtain the correct diffusion signals in each voxel. Note that in this process the b-matrix is not rotated. Also note that log-Euclidean metrics are preferred when the interpolation is performed on the DTs (Arsigny et al., 2006). Finally, the DWIs of the images $\tilde{I}_j$ are averaged to compose an SB atlas in the average space of population. Since the DWI intensities are corrected to represent the diffusion signal in the atlas space, and given the assumption that the coregistration performed well, averaging the DWIs within a single diffusion gradient direction across different subjects is allowed. Subsequently, the diffusion tensors of the atlas are estimated from these averaged DWIs. This atlas construction framework is elucidated in Fig. 1 (I).

Population based atlas method

In the PB atlas framework, non-rigid deformation fields T_{ij} need to be calculated between all images I_i and I_j (with $j = 1, \ldots, N_S$). Note that only N_S $(N_S - 1)/2$ non-rigid deformation fields are calculated, since the transformation of I_i to I_j can be computed as the inverse transformation of I_j to I_i. Subsequently, all N_S images I_i are transformed to the average space of the population with a specific mean deformation field T_i that is calculated as the average deformation of this data set I_i to all other images (as in Eq. (1)). After trilinear interpolation of the DWIs, PPD based tensor reorientation, and recalculation of the DWIs, NS images $\tilde{I}_i$ are constructed in a way that each of them require the least amount of deformation to all other images in the group. Finally, the DWIs of these data sets $\tilde{I}_i$ are averaged to compose the PB atlas (Seghers et al., 2004; Wang et al., 2005). Notice that, in analogy of the SB atlas framework, only one tensor reorientation and one interpolation step are included in the PB atlas method, i.e. after the transformation of the NS images I_i. The construction of the PB atlas is illustrated in Fig. 1 (II).

Atlas evaluation methodology

A general problem in the evaluation of an atlas is to find the optimal representation of a certain group of images. When SB and PB atlases are constructed from the same subject group, it is very difficult

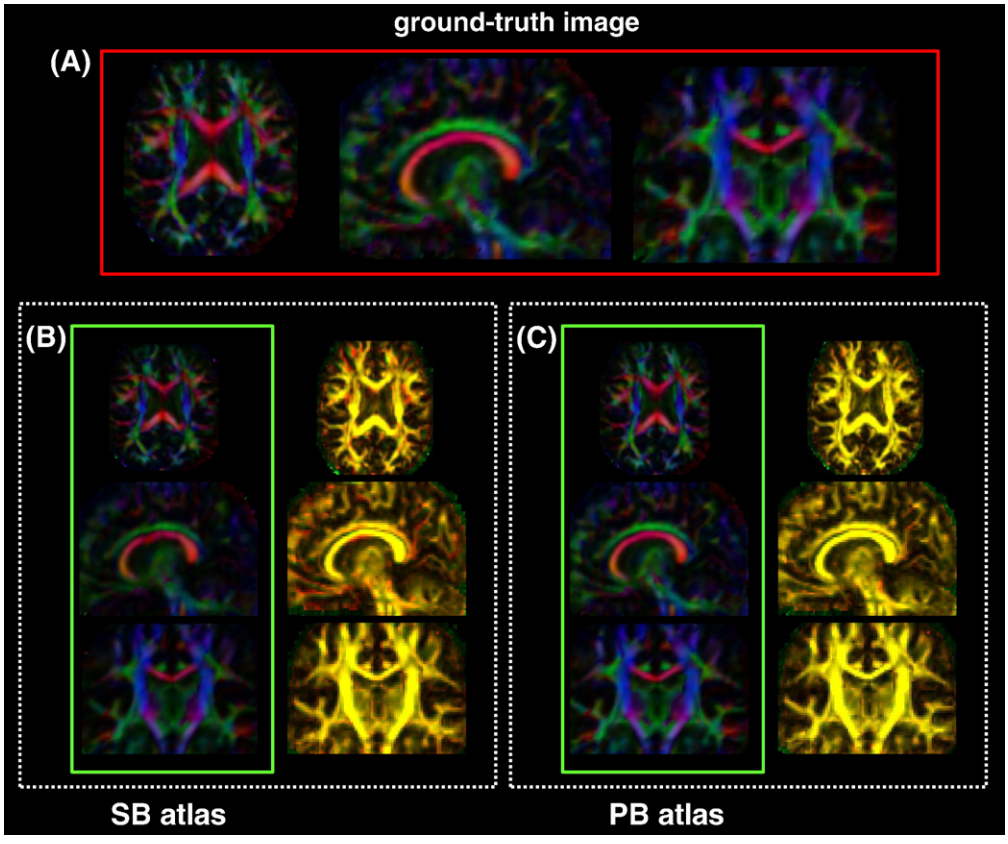

Fig. 3. In (A), an axial, sagittal, and coronal slice of the ground truth image are shown. The color is encoded for the diffusion direction and the image intensity is proportional to the diffusion anisotropy. The same axial, sagittal and coronal slice of the SB and the PB atlas, are visualized in (B) and (C), respectively. In order to evaluate the image correspondence visually, the FA intensity map of the golden standard image is given a red color, whereas the FA intensity map of the atlases are given a green color. Consequently, after overlaying these images, a yellow color appears in the corresponding voxels with similar FA values.

to interpret them visually and to compare them quantitatively. The synthetic data sets that are constructed in this work are based on a single subject DTI data set I, as elucidated in the following steps.

1. First, the DWIs of this single subject data set I are deformed with 10 predefined sinusoidal deformation fields T_i ($i=1, \ldots, 10$). All deformation fields differ from each other in amplitude, frequency, and direction. The maximal relative voxel displacement was 7 voxels.
2. The DTs are calculated from these deformed DWIs and reoriented using the PPD technique (Alexander et al., 2001). It has been demonstrated on a synthetic DTI data set that only a very small tensor reorientation error is made when these smooth, non-rigid deformation field are applied (Van Hecke et al., 2007; Leemans et al., 2005b). Therefore, it can be assumed that the tensors of the deformed images are well aligned with their underlying microstructure.
3. The DWIs are recalculated from these reoriented DTs. In this way, 10 new DT images I_i are defined ($i=1, \ldots, 10$).
4. Next, 10 deformation fields are defined as the inverse of the first 10 transformations ($T_j = T_{j-10}^{-1}, j=11, \ldots, 20$).
5. Analogously to step 2 and 3, 10 deformed DTI data sets I_j were constructed ($j=11, \ldots, 20$). As a result, the total vector sum over all deformation fields equals zero in each voxel: $\sum_{i=1}^{20} T_i = 0$.

Consequently, an atlas that is constructed based on these 20 deformed data sets I_i ($i=1, \ldots, 20$), should closely resemble the original single subject image, since the total vector sum of all deformation fields is zero in each voxel. In this way, the original single subject image is representative for the 20 deformed images. It will therefore be referred to as the ground truth or golden standard image. Notice that, in deforming the single subject DTI data set with sinusoidal deformation fields, the topology, or the architecture of WM connections, is not altered. The potential bias that exists in the SB atlas methodology by selecting a certain initial reference image with unique topological features will therefore not be present in this evaluation method. Furthermore, the quantitative diffusion properties – such as the FA – are the same in all simulated images. After this evaluation, atlases are constructed based on the DTI data sets of 20 different healthy subjects. The quantitative measures that are used for the evaluation of the atlases are expounded in the following section.

Quantitative evaluation measures

The atlas methodologies are compared using both a framework with simulated DTI data sets and actually measured human brain DTI data sets of different subjects. The quantitative measures which are calculated to evaluate the atlases are elucidated in the following paragraphs.

Deformation field difference C

When synthetic data sets are used to construct an atlas, the theoretical deformation fields S_i between the original data set I and the different data sets of the image group are known. Therefore, a value C is computed for each voxel to compare these predefined transformations S_i with the deformation fields that are obtained

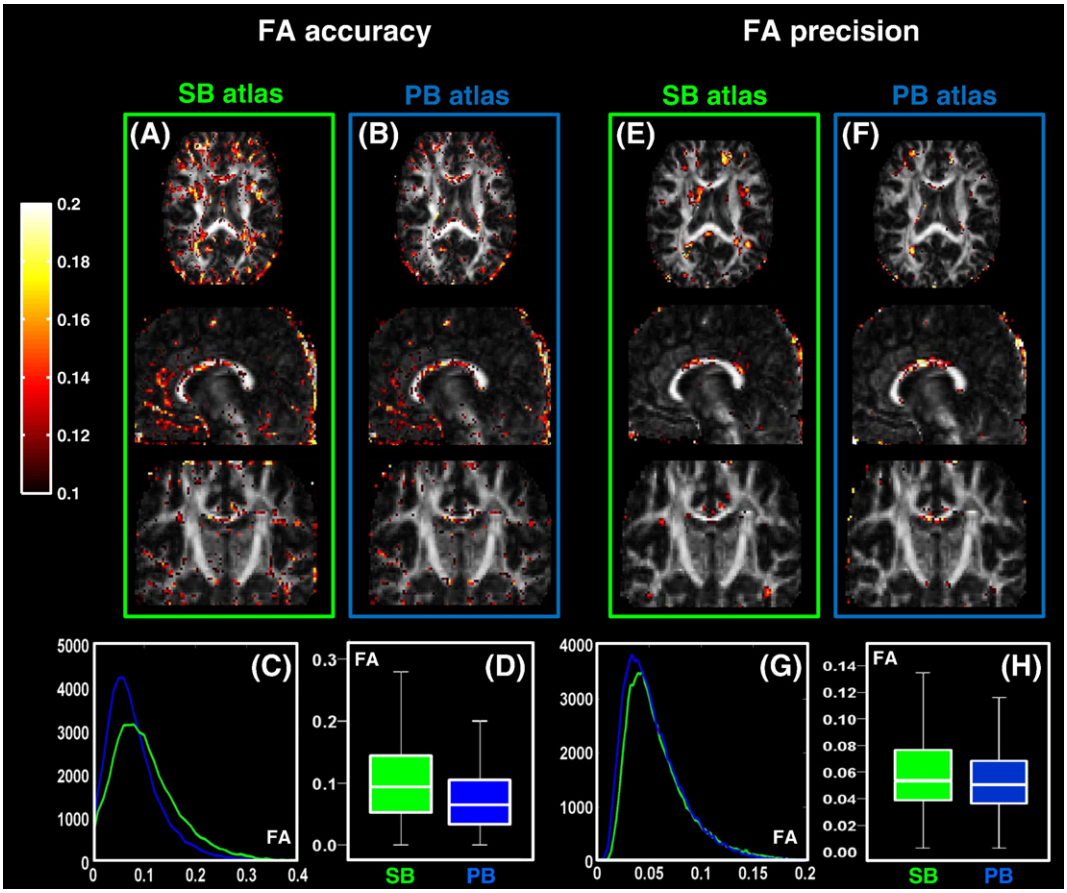

Fig. 4. The absolute value of the FA difference between the ground truth image and the atlases is given. This measure of FA accuracy (i.e., low values represent high accuracy) is visualized for the axial, sagittal, and coronal slice for the SB and the PB atlas in (A) and (B), respectively. In (C) and (D), the FA accuracy histograms and boxplots are displayed. The FA precision, calculated as the FA standard deviation of all images that compose the atlas (i.e., high precision is reflected by low values), is shown in (E) and (F) for the SB and the PB atlas, respectively. The histograms and boxplots of the FA precision are depicted in (G) and (H), whereby the SB and PB atlas results are colored in green and blue, respectively.

during coregistration to transform the simulated data sets to the final atlas space for the different atlas frameworks:

$$C = \frac{\|S-T\|}{\|S\| + \|T\|}. \quad (3)$$

Here, S represents the predefined deformation field and T the deformation field that is obtained to compute the DTI atlas. The latter equals the averaged deformation field T_j in the PB atlas framework and the combination of deformation fields T_{ij} and T_i in the SB atlas framework, when image I_i was the initial reference image. The median of values C across all voxels can then be interpreted as an overall measure of the transformation field correspondence. When this median is 0, the final deformation field exactly equals the theoretical deformation field, representing a perfect spatial alignment. On the other hand, when the median of all Cs is 1, the final deformation field is the opposite of the theoretical deformation field, resulting in the worst alignment. This measure C is computed to compare all simulated deformation fields S_j with the corresponding deformation fields that are used during the atlas construction, resulting in a quantitative measure of the deformation field correspondence for the different atlas frameworks.

Error in FA

The absolute value of the FA difference between an atlas and the golden standard data set is calculated and referred to as the FA accuracy of this atlas. In addition to measuring the FA accuracy of the atlases, the FA precision is calculated for each voxel as the standard deviation of the FA values across the images $\tilde{I}_i$ that are averaged to compose the atlases.

The FA accuracy and FA precision results of the SB and the PB atlas are compared statistically, using a Wilcoxon matched pairs signed rank test. In order to exclude voxels originating from deep GM and CSF in this statistical analysis, only voxels with an FA>0.25 are included in this analysis. Note that only the precision measures can be calculated to compare the atlases of the real subject group. The calculation of the FA accuracy and precision is elucidated in Fig. 2.

Error in overlap of eigenvalue–eigenvector pairs (OVL)

In order to evaluate the orientational DT information of the atlases, the OVL between tensors $D(\lambda,\varepsilon)$ and $D'(\lambda', \varepsilon')$; is calculated (Basser and Pajevic, 2000):

$$\mathrm{OVL} = \frac{1}{N_V}\sum_V \frac{\sum_{i=1}^{3}\lambda_i\lambda_i'\left(\varepsilon_i\cdot\varepsilon_i'\right)^2}{\sum_{i=1}^{3}\lambda_i\lambda_i'}, \quad (4)$$

with N_V the total number of selected WM voxels, and λ_i, λ_i', and ε_i, ε_i' eigenvalue–eigenvector pairs of a corresponding voxel. The minimum value 0 indicates no overlap and the maximum value 1 represents complete overlap of the DTs. In contrast to the FA accuracy and precision, orientational information is included in the OVL evaluation metric.

Analogously to the FA accuracy and precision, the OVL accuracy and OVL precision are defined. The OVL accuracy is calculated for each voxel as the OVL between an atlas and the ground truth image. In order to measure the precision of the orientational correspondence in each voxel, the OVL is calculated between the final atlas result on the one hand and all the deformed images $\tilde{I}_i$ that are averaged to compose this atlas on the other hand. Since they already represent a deviation from the atlas, these OVL measures are subsequently averaged for every voxel to compute the OVL precision for each atlas framework. The OVL accuracy and OVL precision results of the SB and the PB atlas are compared statistically, using a Wilcoxon matched pairs signed

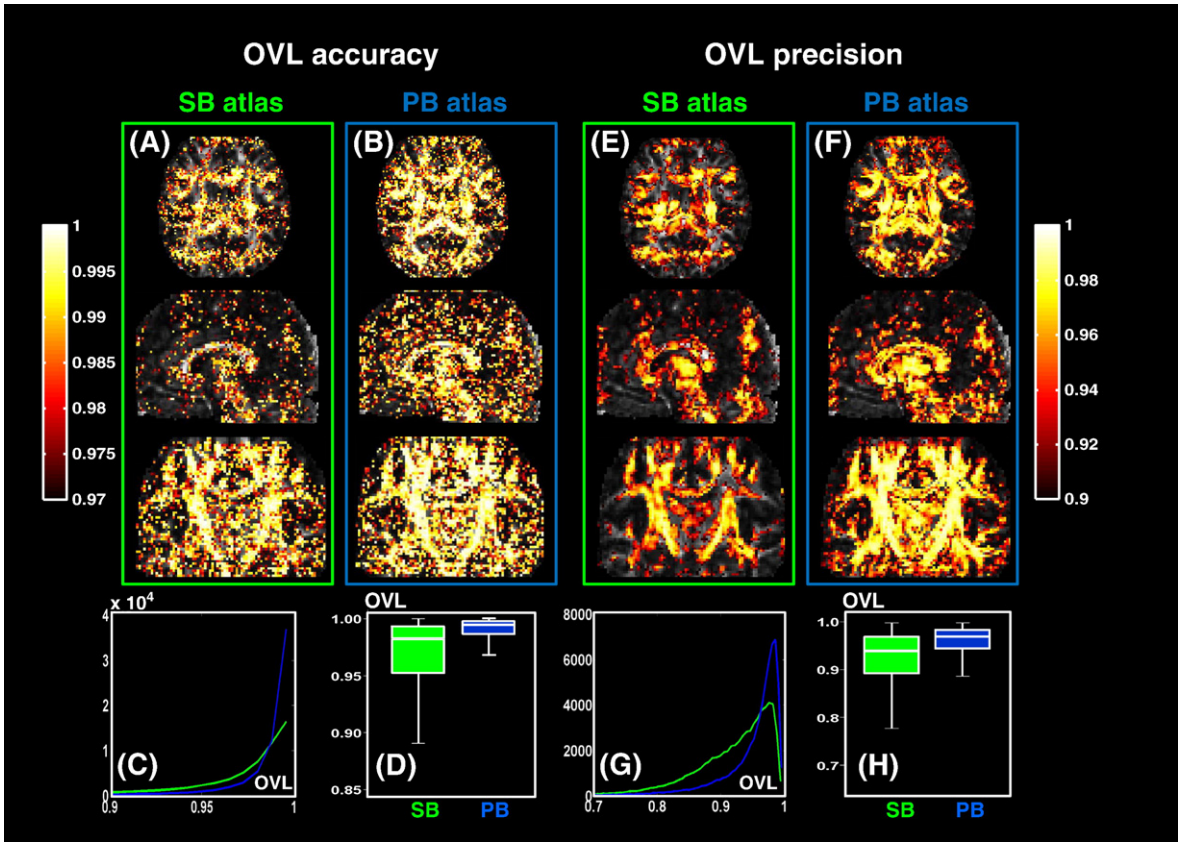

Fig. 5. The overlap of eigenvalue–eigenvector pairs between the DTs of the golden standard image and the DTs of the atlases (high values represent a high accuracy) is presented in each voxel for the SB and the PB atlas in (A) and (B), respectively. In (C) and (D), the OVL accuracy histograms and boxplots are visualized. The OVL precision is calculated as the mean OVL between all images that compose the atlas on the one hand and the atlas itself on the other hand (high values represent a high precision). In (E) and (F), the OVL precision of the SB and the PB atlas is depicted, respectively. The corresponding histograms and boxplots are shown in (G) and (H).

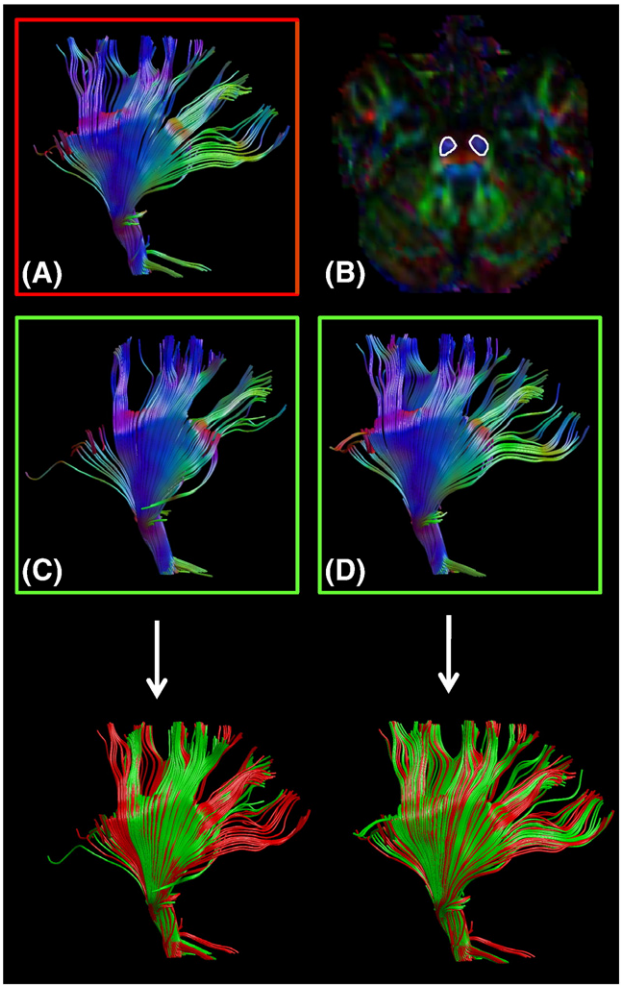

Fig. 6. The cortico-spinal tracts of the ground truth image are visualized in (A). An FA threshold of 0.25 and a maximal angle between consecutive points of 30° are used during the fiber tracking. The seed ROIs are defined on an axial slice, as depicted in (B). The same ROIs were used to define the seeding voxels for the tractography on the atlases. The cortico-spinal tracts of the SB and the PB atlas are shown in (C) and (D), respectively. For a better visual comparison of the tracts, the cortico-spinal tracts of the golden standard data set are given a red color, whereas the cortico-spinal tracts of the different atlases are given a green color.

rank test. The computation of the OVL accuracy and the OVL precision is explained in Fig. 2.

Fiber tract correspondence

Since DT inaccuracies – caused by small, local coregistration errors – are propagated along the fiber bundles, fiber tract correspondence can be used as a more sensitive marker to assess DT atlas correspondence. According to Ding et al. (2003), the similarity between a pair of fibers F_i and F_j can be defined as follows:

$$S_{ij} = R_{cs} e^{-D_{ij}/C}. \quad (5)$$

D_{ij} is the mean Euclidean distance between corresponding segments of the two fiber tracts F_i and F_j (Ding et al., 2003). R_{cs} represents the corresponding segment ratio, defined as the ratio of the length of the corresponding segment L_{cs} to the overall length of the pair of fibers (Ding et al., 2003). Thereby, the corresponding segment L_{cs} is defined as the part of a fiber F_i (i.e. L_i) that has point-wise correspondence to the part of another fiber F_j (i.e. L_i).

$$R_{cs} = \frac{L_{cs}}{L_i + L_j - L_{cs}}. \quad (6)$$

When the corresponding segment ratio is 0, there is no tract overlap. In the case of a perfect overlap of the fiber tracts, the corresponding segment ratio is 1. The coefficient C in Eq. (5) regulates a trade-off between D and R_{cs}. In our work, C is chosen to be 1 voxel width, which is also the case in the article of Ding et al. (2003). Note that similar tract similarity measures have been proposed in other papers (Corouge et al., 2004; O'Donnell and Westin, 2007). In order to obtain a more objective interpretation of the results, an upper limit for the tract similarity measure is created. To this end, the simulated data sets are deformed with a deformation field that is exactly opposite to the theoretical deformation field that was used to compose these images. In this way, an atlas is constructed, using a perfect image alignment, but still including partial volume effects caused by interpolation.

Results

In Table 1, the deformation field difference C, the FA accuracy and precision, and the OVL accuracy and precision are presented for the SB and the PB atlas, which were constructed from the simulated data sets. As can be observed, the deformation field difference is lower for the PB atlas construction framework compared to the SB method ($p < 10^{-6}$). The median and the interquartile range (IQR) of the FA accuracy,

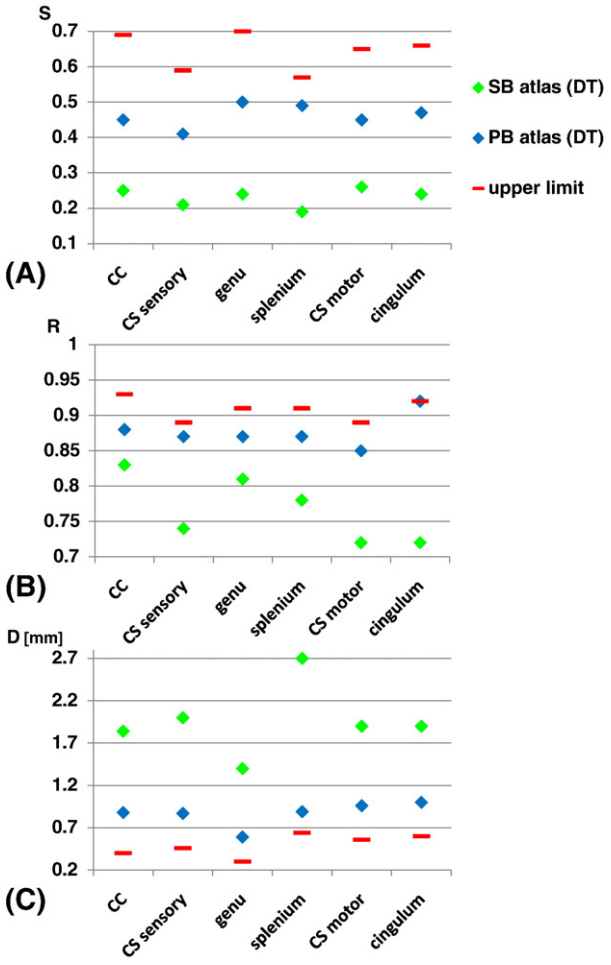

Fig. 7. The quantitative results of the tract correspondence are shown in (A), (B), and (C). In (A), a general tract similarity metric is shown for different WM pathways. A higher value of the tract similarity metric represents a better tract correspondence. The corresponding segment ratio R and the mean Euclidean distance between corresponding segments D are presented in (B) and (C), respectively. Note that an upper limit for the tract similarity measure is added. This upper limit is created by deforming the simulated images with a deformation field that is exactly opposite to the theoretical deformation field that was used to compose these images. The error bars were very small, cluttered the figure, and were therefore not added to the figure.

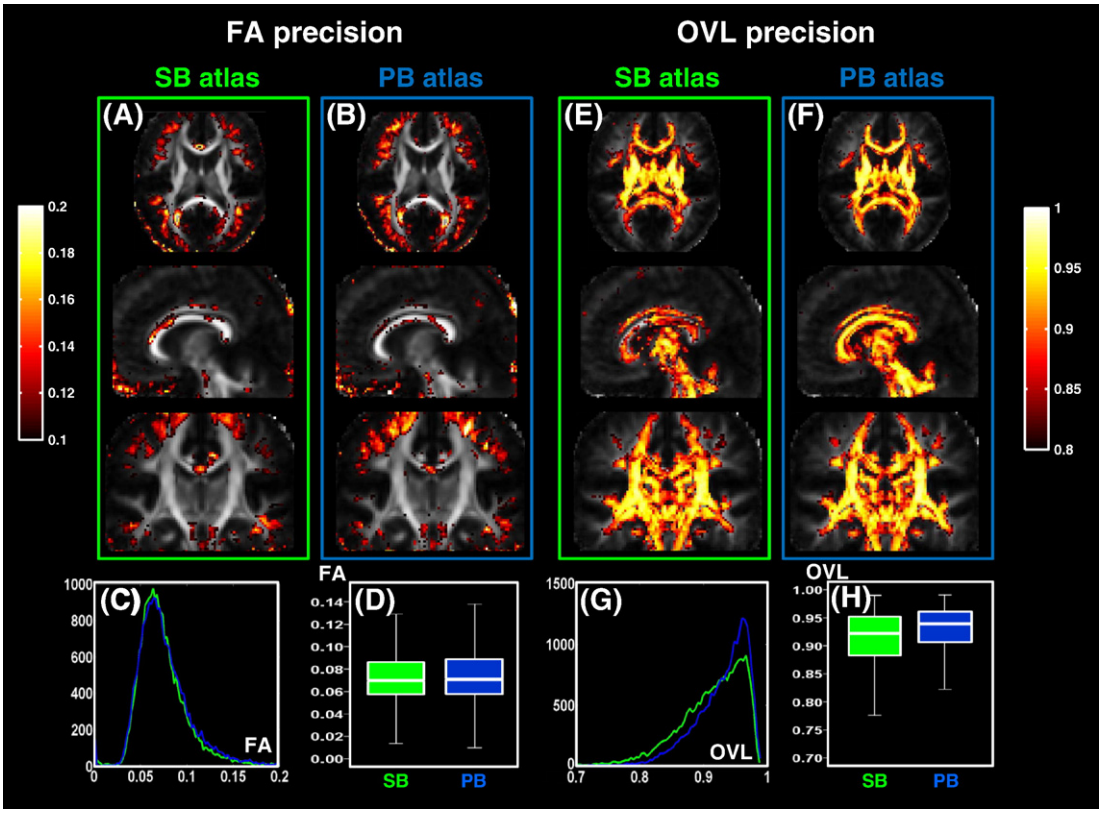

Fig. 8. The FA precision of the inter-subject SB and PB atlas are displayed in (A) and (B), respectively. The FA precision is superimposed on an axial, sagittal, and coronal slice of the PB atlas. In (C) and (D), the corresponding FA precision histograms and boxplots are depicted. The inter-subject OVL precision is visualized for the SB and the PB atlas in (E) and (F), respectively. In (F) and (G), the OVL precision histograms and boxplots are presented.

FA precision, OVL accuracy, and OVL precision are also displayed in Table 1. These results are also visualized in Figs. 4 and 5.

An axial, sagittal, and coronal FA slice of the ground truth image, the SB, and the PB atlas are depicted in Figs. 3 (A), (B), and (C), respectively. The image correspondence can be evaluated visually, by overlaying the red colored FA intensity map of the golden standard data set and the green colored FA intensity maps of the atlases. As can be observed in Fig. 3, the highest spatial correspondence with the ground truth image is obtained by the PB atlas.

In order to study the FA accuracy of the different atlases, the absolute value of the FA difference between the atlases and the golden standard data set is calculated for each voxel as explained in Fig. 2, and scaled between 0.1 and 0.2. The FA accuracy of the SB and the PB atlas are displayed in Figs. 4 (A) and (B), respectively. The highest FA accuracy or the lowest FA difference is detected for the PB atlas, as shown qualitatively by the histograms and boxplots in Figs. 4 (C) and (D), respectively. The Wilcoxon matched pairs signed rank test demonstrates that this FA accuracy difference is statistically significant ($p<10^{-15}$). The FA precision results of the SB and the PB atlas are displayed in Figs. 4 (E) and (F), respectively. Analogously to the FA accuracy results, the PB atlas outperforms the SB atlas with respect to the FA precision. Histograms and boxplots confirm these findings (see Figs. 4 (G) and (H)), which are statistically significant ($p<10^{-10}$).

In order to evaluate the preservation of the orientational information during the atlas construction, the OVL accuracy is measured at each voxel (see Fig. 5). A higher OVL accuracy is observed for the PB atlas compared to the SB atlas (see Figs. 5 (A), (B), (C), and (D)). Analogously to the OVL accuracy results, the highest OVL precision is observed for the PB atlas, as illustrated in Figs. 5 (E), (F), (G), and (H). These differences in the OVL accuracy and precision are statistically significant ($p<10-10$).

In Fig. 6 (A), the cortico-spinal tracts of the golden standard image are visualized. The ROIs that are used to obtain these tracts are shown on an axial slice in Fig. 6 (B). These ROIs are also utilized to define the fiber tractography seed points of the atlases (see Figs. 6 (B) and (C)). In Figs. 6 (B) and (C), the cortico-spinal tracts of the SB and the PB atlas are shown, respectively. An FA threshold of 0.25 and a maximal angle between consecutive points of 30 are used for fiber tracking (Basser et al., 2000). In order to allow a better visual comparison of the fiber pathways, the green colored cortico-spinal tracts of the ground truth image and the red colored cortico-spinal tracts of the different atlases are overlaid. The tract similarity measure of Ding et al. (2003) is evaluated for several WM tracts to quantify the tract correspondence (Fig. 7). The corresponding segment ratio R and the mean Euclidean distance between corresponding segments D are presented in Figs. 7 (B) and (C), respectively. The quantitative tract correspondence measures confirm the voxel-based tensor correspondence results of Fig. 5 and the visual tract results of Fig. 6, demonstrating the highest tract accuracy for the PB tracts.

In Fig. 8, the inter-subject FA precision results of the SB and the PB atlas are superimposed on the axial, sagittal, and coronal FA slice of the PB atlas, as presented in (A) and (B), respectively. Figs. 8 (C) and (D) shows the corresponding histogram and boxplot. As can be seen in Figs. 8 (E), (F), (G), and (H), the OVL precision of the PB atlas is higher compared to the OVL precision of the SB atlas ($p<10^{-10}$).

The tractography results of the corpus callosum are shown for 20 subjects in Fig. 9 (A). The callosal fiber tracts reconstructed from the SB and the PB atlas are visualized in Figs. 9 (B), (C), respectively.

Discussion

Recently, Jones et al. (2005, 2007) and Zhang et al. (2007) demonstrated the dependence of VBM results on the selection of

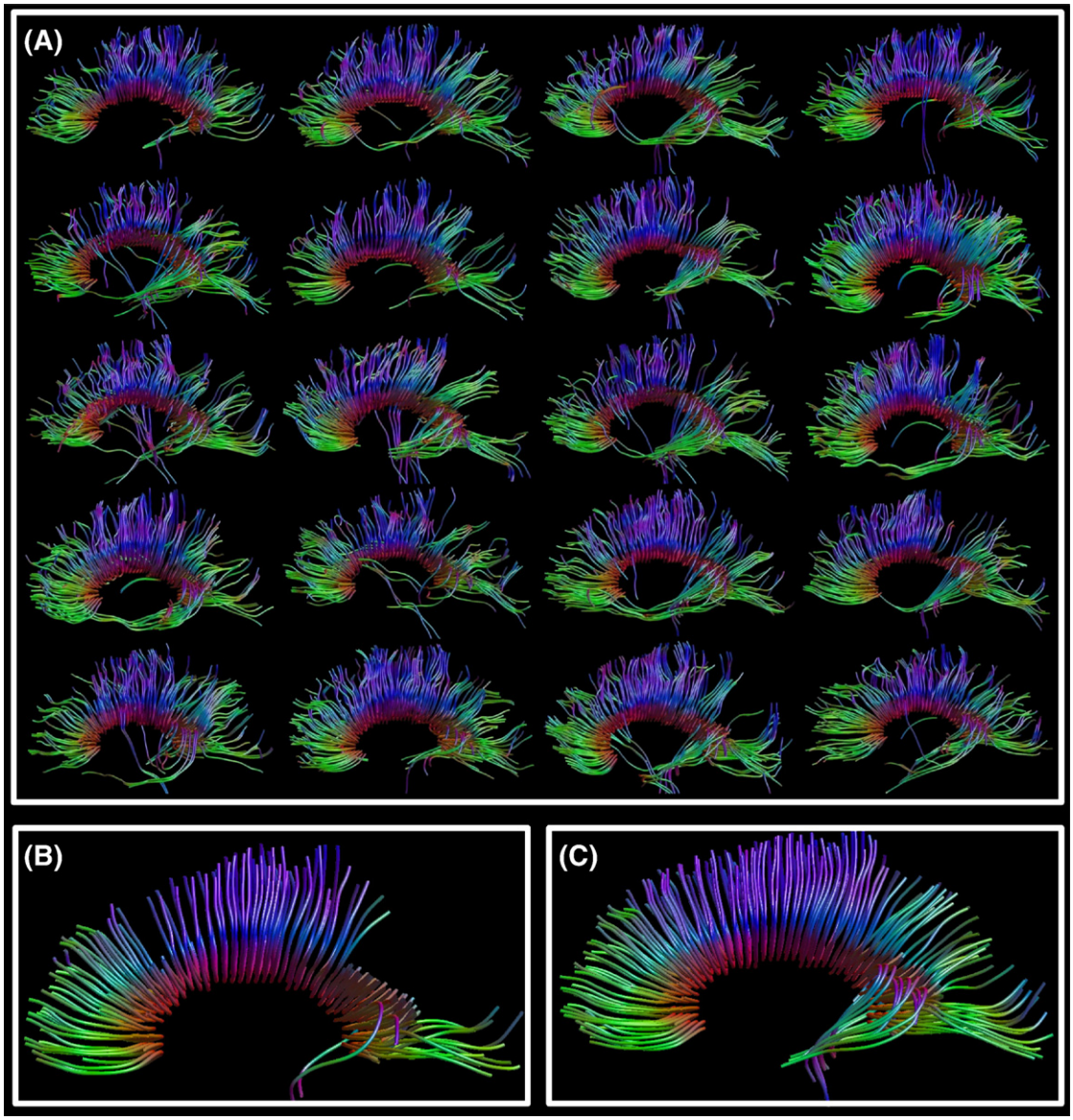

Fig. 9. In (A), the corpus callosum tracts of 20 different subjects are displayed. The corpus callosum tracts of the SB and the PB atlas, constructed from these 20 images, are shown in (B) and (C), respectively.

the smoothing kernel, coregistration technique, and other choices in the in the pipeline of a VBM analysis. Furthermore, it has been shown in the research of cortical atrophy that the VBM results depend on the selection of the reference system (Shen et al., 2005, 2007). In order to enhance the reliability of a VBM analysis of DT images, a study-specific DTI atlas should be constructed which can be regarded as a good representation of the subject group and which contains the relevant diffusion information in a reliable way. Although, the problem of atlas construction has been extensively studied and validated for scalar-valued images, similar studies for DT images are lacking (Wang et al., 2005; Kochunov et al., 2001; Rohlfing et al., 2004; Joshi et al., 2004; Lorenzen et al., 2006; Studholme and Cardenas, 2004; Christensen et al., 2006).

In many VBM studies of DT images, an affine atlas is utilized as the reference image. However, since the data sets that are averaged to construct an affine atlas are only globally aligned, relevant, local diffusion information can be partially lost. In our work, the developed non-rigid atlases were also compared with an affine atlas (results not shown). As expected, the non-rigid atlases outperformed the affine atlas with respect to the accuracy and precision of the spatial and orientational diffusion information.

Many of the DTI atlases in VBM studies are based on the coregistration of T_2 weighted, non- diffusion weighted images, or FA maps. Consequently, the tensor information is not reliably present in the atlas, since it is not fully taken into account during the image alignment. As a result, this tensor information cannot be used during the image alignment of different data sets to such an atlas in a VBM analysis.

In our work, the full DT was incorporated during the coregistration. However, similar atlases were also constructed using FA based image alignment (results not shown). We demonstrated using the simulated data sets that the accuracy and precision of these atlases were significantly lower compared to the atlases that were constructed using the full DT during coregistration. As expected, the OVL accuracy and precision decreased when only FA information was used for coregistration. Many VBM studies of DT images incorporate structural T_2 weighted or non-diffusion weighted images to drive the image alignment during the atlas construction or the VBM analysis, thereby discarding valuable WM information, which is reflected by the diffusion tensor.

In almost all VBM studies of DT images, the standard MNI atlas is utilized as the reference system (Borroni et al., 2007; Seok et al., 2007;

Snook et al., 2007). Since this is not a study-specific atlas, large deformation fields might be necessary to warp the data sets of the subject group to this atlas. Consequently, image alignment inaccuracies might be introduced, which can affect the accurateness of the VBM results. In other studies, the reference system is based on a detailed representation of a single subject's anatomy, as is the case in the SB method (Park et al., 2003, 2004; Jones et al., 2002). The chosen data set then acts as a template to which the images of other subjects are coregistered. Subsequently, the transformed images of all subjects in the group are averaged, resulting in a new atlas. Thereafter, this atlas is transformed to a more representative atlas space, to minimize the magnitude of the deformation fields between the data sets of the subject group and the atlas. However, the choice of one image as a template unavoidably biases the atlas topology because of the substantial inter-subject variations in brain anatomy and WM morphology (Wang et al., 2005).

In this work, the optimal initial reference image for the SB approach was selected by evaluating the image correspondence – as calculated by the MI – between all data sets I_j of the image group and the golden standard data set. Obviously, this way of selecting the optimal initial reference image is not possible in an inter-subject setting, since no ground truth is available. One possible solution to this problem is to use an iterative approach for the SB atlas construction, whereby in the second iteration the atlas result of the first iteration is employed as the reference image, as suggested by Guimond et al. (2000). This strategy was also applied in this work, but did not lead to significant improvement of the final atlas. Another possibility to find the most typical subject for a given image group is to define the image that has a minimal mean distance to all other images — as calculated from the averaged deformation fields of each data set to all other data sets (Smith et al., 2006). In this way, the amount of warping of all images of the subject group to the initial reference data set is minimized. In order to calculate this mean distance to all other image for every data set, all images have to be aligned to each other, making this approach as computational intensive as the PB atlas method. Since, in our study, all images were aligned to each other to construct the PB atlas, this strategy of finding the optimal initial reference image was applied in the SB atlas framework.

In contrast to the SB method, the PB framework is unbiased towards the brain topology of a single subject. However, the PB atlas construction method is computational intensive, since deformation fields are calculated between all subjects. On a Pentium(R) D CPU 3 GHz with 2 GB of RAM, and using a Matlab 7 platform (MathWorks, Natick, Mass), the computation time for the PB atlas for 20 data sets was approximately 12 h. Computation time is approximately proportional with the square of the number of subjects.

Recently, group-based atlas frameworks, which consider all subjects in the population simultaneously, have been introduced to construct a population specific atlas. These methods might be advantageous in terms of finding the global optimum, since all data sets are iteratively optimized to minimize the discrepancies between these images. In the work by Studholme and Cardenas (2004), a cost function is optimized with the aim of maximizing the similarity between all images, while penalizing displacement of the reference space from the average shape. Christensen et al. (2006) present a method for synthesizing average 3*D* anatomical shapes using deformable templates based on averaging transformations. Joshi et al. (2004) developed an algorithm for the simultaneous registration of subjects using large deformation diffeomorphisms. Goodlett et al. (2006) applied this framework of Joshi et al. (2004) to scalar diffusion measures. Lorenzen et al. (2006) also adapted the large deformation diffeomorphism framework for group-based coregistration, but utilized a probabilistic segmentation of the images instead of the images intensities.

An important limitation in the evaluation of atlases and image coregistration is the lack of knowledge regarding the optimal representation of a given group of subjects. One approach of evaluating image correspondence is to define landmark points in different data sets. However, besides its labor-intensity, this method has a restricted reproducibility due to the intra- and inter-observer variability in the placement of the landmarks. In addition, it is hard to capture the complex 3D anatomical structures by the placement of landmarks on 2D slices. Moreover, this validation analysis is restricted to the anatomical structures that are delineated. Finally, this method can only provide information regarding the spatial accuracy of the image alignment, and not regarding the accuracy and validity of the orientational DT information in the atlas. Since recently developed coregistration techniques are incorporating multi-component DT information to obtain an optimal image alignment, it is important that this DT information is accurately represented in the atlas. In this context, the accuracy and precision of orientational DT information needs to be evaluated as well.

In order to tackle the limitations of the landmark based evaluation approach, a ground truth method was introduced, which allows one to evaluate the accuracy and precision of the spatial and orientational DT information in every brain voxel. Furthermore, since all data sets are constructed by deforming the same single subject image with different deformation fields, the unknown inter-subject variability of the diffusion properties cannot introduce a bias in this evaluation method. A reduced accuracy and precision of the spatial and orientational diffusion properties in the atlases are therefore produced by spatial and orientational image alignment inaccuracies, interpolation artifacts, or the atlas construction framework, and not by variances in the topology and the diffusion measures across subjects. Consequently, the higher FA accuracy and precision that were observed in the PB atlas reflect the higher robustness of the PB atlas method against imperfect image alignment, compared to the SB approach (see Table 1). This better spatial image alignment in the PB method and the use of averaged deformation fields to transform the data sets in the PB atlas framework, result in a higher OVL accuracy and precision in the PB atlas compared to the SB atlas. These averaged deformation fields are less susceptible to tensor reorientation inaccuracies which are caused by small spatial image alignment imperfections (Van Hecke et al., 2007). In this context, the DTI coregistration approaches of Cao et al. (2005, 2006) and of Zhang et al. (2006), which incorporate the tensor reorientation as part of the image alignment optimization, might improve the orientational accuracy and precision of the DTI atlas.

In order to validate the different atlas frameworks for acquired brain DTI data sets, inter-subject atlases were constructed based on the data sets of 20 healthy subjects. Obviously, the presence of inter-subject variability of the WM topology and the diffusion properties complicate the evaluation of the inter-subject atlases. In Fig. 9, the callosal fiber tracts of the atlases were compared visually with the callosal pathways of the different subjects that compose the inter-subject image group. Qualitatively, the tract results of the PB atlas appear to provide the best expected averaged representation of the corpus callosum of these 20 subjects.

In summary, different strategies for constructing WM atlases from a set of DT images have been compared in this article. To the best of our knowledge, this work represents the first attempt at understanding the relative merits of two atlas construction strategies which were previously developed for scalar-valued images. The spatial and orientational diffusion information of these atlases were evaluated using both simulated and real DTI data sets. Our results indicate that the PB atlas provides the most robust representation for a group of subjects. We believe that the use of the proposed study-specific, population based DT atlas with a reliable incorporation of all DT information, can reduce the image alignment inaccuracies and thus increase the reliability of the statistical tests in a VBM analysis.

References

Abe, O., Yamada, H., Masutani, Y., Aoki, S., Kunimatsu, A., Yamasue, H., Fukuda, R., Kasai, K., Hayashi, N., Masumoto, T., Mori, H., Soma, T., Ohtomo, K., 2004. Amyotrophic lateral sclerosis: diffusion tensor tractography and voxel-based analysis. NMR Biomed. 17 (6), 411–416.

Alexander, D.C., Pierpaoli, C., Basser, P.J., Gee, J.C., 2001. Spatial transformations of diffusion tensor magnetic resonance images. IEEE Trans. Med. Imaging. 20 (11), 1131–1139.

Ardekani, S., Sinha, U., 2006. Statistical representation of mean diffusivity and fractional anisotropy brain maps of normal subjects. J. Magn. Reson. Imaging 24 (6), 1243–1251.

Arsigny, V., Fillard, P., Pennec, X., Ayache, N., 2006. Log-Euclidean Metrics for Fast and Simple Calculus on Diffusion Tensors. Magn. Reson. Med. 56 (2), 411–421.

Ashburner, J., Friston, K., 2000. Voxel-based morphometry — the methods. NeuroImage 11, 805–821.

Bammer, R., Acar, B., Moseley, M.E., 2003. In vivo MR tractography using diffusion imaging. Eur. J. Radiol. 45 (3), 223–234.

Basser, P.J., Pierpaoli, C., 1996. Microstructural and physiological features of tissues elucidated by quantitative-diffusion-tensor MRI. J. Magn. Reson. B. 111 (3), 209–219.

Basser, P.J., Pajevic, S., 2000. Statistical artifacts in diffusion tensor MRI (DT-MRI) caused by background noise. Magn. Reson. Med. 44 (1), 41–50.

Basser, P.J., Mattiello, J., Le Bihan, D., 1994. MR diffusion tensor spectroscopy and imaging. Biophys. J. 66 (1), 259–267.

Basser, P.J., Pajevic, S., Pierpaoli, C., Duda, J., Aldroubi, A., 2000. In vivo fiber tractography using DT-MRI data. Magn. Reson. Med. 44, 625–632.

Beaulieu, C., 2002. The basis of anisotropic water diffusion in the nervous system — a technical review. NMR Biomed. 15 (7–8), 435–455.

Bookstein, F.L., 2001. Voxel-based morphometry should not be used with imperfectly registered images. Neuroimage 14 (6), 1454–1462.

Borroni, B., Brambati, S.M., Agosti, C., Gipponi, S., Bellelli, G., Gasparotti, R., Garibotto, V., Di Luca, M., Scifo, P., Perani, D., Padovani, A., 2007. Evidence of white matter changes on diffusion tensor imaging in frontotemporal dementia. Arch. Neurol. 64 (2), 246–251.

Bürgel, U., Amunts, K., Hoemke, L., Mohlberg, H., Gilsbach, J.M., Zilles, K., 2006. White matter fiber tracts of the human brain: three-dimensional mapping at microscopic resolution, topography and intersubject variability. NeuroImage 29 (4), 1092–1105.

Cao, Y., Miller, M.I., Winslow, R.L., Younes, L., 2005. Large deformation diffeomorphic metric mapping of vector fields. IEEE Trans. Med. Imaging 24 (9), 1216–1230.

Cao, Y., Miller, M.I., Mori, S., Winslow, R.L., Younes, L., 2006. Diffeomorphic matching of diffusion tensor images. Conference on Computer Vision and Pattern Recognition Workshop, 67.

Christensen, G.E., Johnson, H.J., Vannier, M.W., 2006. Synthesizing average 3D anatomical shapes. NeuroImage 32, 146–158.

Corouge, I., Gouttard, S., Gerig, G., 2004. Towards a shape model of white matter fiber bundles using diffusion tensor. MRI 344–347.

D'Agostino, E., Maes, F., Vandermeulen, D., Suetens, P., 2003. A viscous fluid model for multimodal non-rigid image registration using mutual information. Med. Image Anal. 7 (4), 565–575.

Ding, Z., Gore, J.C., Anderson, A.W., 2003. Classification and quantification of neuronal fiber pathways using diffusion tensor MRI. Magn. Reson. Med. 49 (4), 716–721.

Douaud, G., Smith, S., Jenkinson, M., Behrens, T., Johansen-Berg, H., Vickers, J., James, S., Voets, N., Watkins, K., Matthews, P.M., James, A., 2007. Anatomically related grey and white matter abnormalities in adolescent-onset schizophrenia. Brain 130, 2375–2386.

Dougherty, R.F., Ben-Shachar, M., Deutsch, G., Potanina, P., Bammer, R., Wandell, B.A., 2005. Occipital–callosal pathways in children: validation and atlas development. Ann. N. Y. Acad. Sci. 1064, 98–112.

Fellgiebel, A., Albrecht, J., Dellani, P.R., Schermuly, I.P.S., Muller, M.J., 2007. Quantification of brain tissue alterations in Fabry disease using diffusion-tensor imaging. Acta Paediatr. Suppl. 96 (455), 33–36.

Goodlett, C., Davis, B., Jean, R., Gilmore, J., Gerig, G., 2006. Improved correspondence for DTI population studies via unbiased atlas building. MICCAI 260–267.

Guimond, A., Meunier, J., Thirion, J.P., 2000. Average brain models: a convergence study. Comput. Vision Imag. Understand 77, 192–210.

Jones, D.K., 2004. The effect of gradient sampling schemes on measures derived from diffusion tensor MRI: a Monte Carlo study. Magn. Reson. Med. 51, 807–815.

Jones, D.K., Griffin, L.D., Alexander, D.C., Catani, M., Horsfield, M.A., Howard, R., Williams, S.C.R., 2002. Spatial normalization and averaging of diffusion tensor MRI data sets. NeuroImage 17 (2), 592–617.

Jones, D.K., Symms, M.R., Cercignani, M., Howarde, R.J., 2005. The effect of filter size on VBM analyses of DT-MRI data. NeuroImage 26 (2), 546–554.

Jones, D.K., Chitnis, X.A., Job, D., Khong, P.L., Leung, L.T., Marenco, S., Smith, S.M., Symms, M.R., 2007. What happens when nine different groups analyze the same DT-MRI data set using voxel-based methods? Proc. ISMRM 15th Annual Meeting, Berlin, 74.

Joshi, S., Davis, B., Jomier, M., Gerig, G., 2004. Unbiased diffeomorphic atlas construction for computational anatomy. NeuroImage 23, S151–S160.

Kochunov, P., Lancaster, J.L., Thompson, P., Woods, R., Mazziotta, J., Hardies, J., Fox, P., 2001. Regional spatial normalization: toward an optimal target. J. Comput. Assist. Tomogr. 25 (5), 805–816.

Kyriakopoulos, M., Vyas, N.S., Barker, G.J., Chitnis, X.A., Frangou, S., 2007. A diffusion tensor imaging study of white matter in early-onset schizophrenia. Biol. Psychiatry 63 (5), 519–523.

Leemans, A., Sijbers, J., Parizel, P.M., 2005a. A graphical toolbox for exploratory diffusion tensor imaging and fiber tractography. 14th Annual Meeting — Section for Magnetic Resonance Technologists.

Leemans, A., Sijbers, J., Verhoye, M., Van der Linden, A., Van Dyck, D., 2005b. Mathematical framework for simulating diffusion tensor MR neural fiber bundles 53 (4), 944–953.

Lorenzen, P., Prastawa, M., Davis, B., Gerig, G., Bullitt, E., Joshi, S., 2006. Multi-modal image set registration and atlas formation. Med. Image Anal. 10 (3), 440–451.

Maes, F., Collignon, A., Vandermeulen, D., Marchal, G., Suetens, P., 1997. Multimodality image registration by maximization of mutual information. IEEE Trans. Med. Imaging. 16 (2), 187–198.

Muller, H.P., Unrath, A., Ludolph, A.C., Kassubek, J., 2007. Preservation of diffusion tensor properties during spatial normalization by use of tensor imaging and fibre tracking on a normal brain database. Phys. Med. Biol. 52 (6), N99–N109.

O'Donnell, L.J., Westin, C.-F., 2007. Automatic tractography segmentation using a high-dimensional white matter atlas. IEEE Trans. Med. Imaging 26 (11), 1562–1575.

Pagani, E., Filippi, M., Rocca, M.A., Horsfield, M.A., 2005. A method for obtaining tract-specific diffusion tensor MRI measurements in the presence of disease: application to patients with clinically isolated syndromes suggestive of multiple sclerosis. NeuroImage 26 (1), 258–265.

Park, H.-J., Kubicki, M., Shenton, M.E., Guimond, A., McCarley, R.W., Maier, S.E., Kikinis, R., Jolesz, F.A., Westin, C.-F., 2003. Spatial normalization of diffusion tensor MRI using multiple channels. NeuroImage 20 (4), 1995–2009.

Park, H.-J., Westin, C.-F., Kubicki, M., Maier, S.E., Niznikiewicz, M., Baer, A., Frumin, M., Kikinis, R., Jolesz, F.A., McCarley, R.W., Shenton, M.E., 2004. White matter hemisphere asymmetries in healthy subjects and in schizophrenia: a diffusion tensor MRI study. NeuroImage 23 (1), 213–223.

Rohlfing, T., Brandt, R., Menzel, R., Maurer, C.R., 2004. Evaluation of atlas selection strategies for atlas-based image segmentation with application to confocal microscopy images of bee brains. Neuroimage 21 (4), 1428–1442.

Rovaris, M., Filippi, M., 2007. Diffusion tensor MRI in multiple sclerosis. J. Neuroimaging 17, 27S–30S.

Seghers, D., D'Agostino, E., Maes, F., Vandermeulen, D., Suetens, P., 2004. Construction of a brain template from MR images using state-of-the-art registration and segmentation techniques. LNCS 3216, 696–703.

Seok, J.H., Park, H.J., Chun, J.W., Lee, S.K., Cho, H.S., Kwon, J.S., Kim, J.J., 2007. White matter abnormalities associated with auditory hallucinations in schizophrenia: a combined study of voxel-based analyses of diffusion tensor imaging and structural magnetic resonance imaging. Psychiatry Res. 156 (2), 93–104.

Shen, S., Szameitat, A.J., Sterr, A., 2005. A template effect study on voxel-based morphometry in statistic parametric mapping. Conf. Proc. IEEE Eng. Med. Biol. Soc 3, 3051–3054.

Shen, S., Szameitat, A.J., Sterr, A., 2007. Vbm lesion detection depends on the normalization template: a study using simulated atrophy. Magn. Reson. Imaging 25 (10), 1385–1396.

Smith, S.M., Jenkinson, M., Johansen-Berg, H., Rueckert, D., Nichols, T.E., Mackay, C.E., Watkins, K.E., Ciccarelli, O., Cader, M.Z., Matthews, P.M., Behrens, T.E., 2006. Tract-based spatial statistics: voxelwise analysis of multi-subject diffusion data. NeuroImage 4 (31), 1487–1505.

Snook, L., Paulson, L.-A., Roy, D., Phillips, L., Beaulieu, C., 2005. Diffusion tensor imaging of neurodevelopment in children and young adults. NeuroImage 26 (4), 1164–1173.

Snook, L., Plewes, C., Beaulieu, C., 2007. Voxel based versus region of interest analysis in diffusion tensor imaging of neurodevelopment. NeuroImage 34 (1), 243–252.

Studholme, C., Cardenas, V., 2004. A template free approach to volumetric spatial normalisation of brain anatomy. Pattern Recognition Letters 25 (10), 1191–1202.

Talairach, J., Tournoux, P., 1998. Co-planar Stereotaxic Atlas of the Human Brain. 3-dimensional Proportional System: An Approach to Cerebral Imaging. Thieme Medical Publishers, New York.

Toosy, A.T., Werring, D.J., Orrell, R.W., Howard, R.S., King, M.D., Barker, G.J., Miller, D.H., Thompson, A.J., 2003. Diffusion tensor imaging detects corticospinal tract involvement at multiple levels in amyotrophic lateral sclerosis. J. Neurol. Neurosurg. Psychiatry. 74, 1250–1257.

Van Hecke, W., Leemans, A., D'Agostino, E., De Backer, S., Vandervliet, E., Parizel, P.M., Sijbers, J., 2007. Nonrigid coregistration of diffusion tensor images using a viscous fluid model and mutual information. IEEE Trans. Med. Imaging. 26 (11), 1598–1612.

Wakana, S., Jiang, H., Nagae-Poetscher, L.M., van Zijl, P.C.M., Mori, S., 2004. Fiber tract-based atlas of human white matter anatomy. Radiol. 230 (1), 77–87.

Wang, Q., Seghers, D., D'Agostino, E., Maes, F., Vandermeulen, D., Suetens, P., Hammers, A., 2005. Construction and validation of mean shape atlas templates for atlas-based brain image segmentation. LNCS 3565, 689–700.

Zhang, H., Yushkevich, P.A., Alexander, D.C., Gee, J.C., 2006. Deformable registration of diffusion tensor MR images with explicit orientation optimization. Med. Image Anal. 10 (5), 764–785.

Zhang, H., Avants, B.B., Yushkevich, P.A., Woo, J.H., Wang, S., McCluskey, L.F., Elman, L.B., Melhem, E.R., Gee, J.C., 2007. High-dimensional spatial normalization of diffusion tensor images improves the detection of white matter differences: an example study using amyotrophic lateral sclerosis. IEEE Trans. Med. Imaging 26 (11), 1585–1597.